26th AIAA Applied Aerodynamics Conference
18 - 21 August 2008, Honolulu, Hawaii

AIAA 2008-7340

Time Spectral Method for Rotorcraft Flow with Vorticity Confinement

Nawee Butsuntorn* and Antony Jameson†
Stanford University, Stanford, California, 94305, U.S.A.

This paper follows up on the authors' recent paper.[1] It is shown here that it is possible to obtain reasonable improvement in the results utilizing Vorticity Confinement method. The previous paper has shown that using the Time Spectral method can increase convergence in forward flight calculations by up to two orders of magnitude compared to the traditional Backward Difference Formula (BDF). With the addition of a new boundary condition for the periodic planes, Euler and RANS forward flight calculations can now be done using only one sector of the blade, and thus further improve convergence by a factor of N for an N-bladed rotor,

I. Introduction

It has been shown that the Time Spectral method can significantly reduce the computational cost for periodic problems such as pitching airfoils and wings (Gopinath & Jameson[2]), and rotorcraft flow simulation (Butsuntorn & Jameson[1]). The latter paper has shown that the Time Spectral method can be up to two orders of magnitude cheaper than the traditional Backward Difference Formula (Jameson, 1991[3]) when used for rotorcraft simulation in forward flight. Further, Butsuntorn & Jameson[1] developed a new formulation for Vorticity Confinement for transonic flow calculation, which showed promising results for three-dimensional transonic Euler calculations on an untapered, untwisted NACA 0012 wing.

The current work utilizes a new formulation for the periodic boundaries first proposed by Ekici *et al.*[4] Using this boundary condition, only one sector of a rotor is needed for forward flight calculation. This makes the calculation cheaper by a factor of N where N is the number of blades in a given rotor. Additionally, with the application of Vorticity Confinement method using a new formulation, it is shown that the vortical structure stemmed from the blades in both hover and forward flight can be prevented from diffusing too quickly in the coarse mesh regions.

II. Governing Equations and Discretization

Let p, ρ, E and H denote the pressure, density, total energy and total enthalpy of the fluid. The Cartesian coordinates and velocity components are denoted by x_1, x_2, x_3 and u_1, u_2, u_3 respectively. Einstein notation is used to simplify the presentation of the equations where the summation is implied with the repeated index.

Consider the flow equations without the body force in integral form:

$$\frac{\partial}{\partial t}\int_\Omega \mathbf{w}\,\mathrm{d}\mathcal{V} + \oint_{\partial\Omega} \mathbf{f}_j \cdot \mathbf{n}\,\mathrm{d}\mathcal{S} = 0 \tag{1}$$

*Doctoral Candidate, Department of Mechanical Engineering, Stanford University, AIAA Student Member.
†Thomas V. Jones Professor of Engineering, Department of Aeronautics & Astronautics, Stanford University, AIAA Member.

where $\mathbf{w}$ is the state vector with the following components:

$$\mathbf{w} = \begin{bmatrix} \rho \\ \rho u_1 \\ \rho u_2 \\ \rho u_3 \\ \rho E \end{bmatrix}.$$

The flux $\mathbf{f}_j$ can be split into the convective and viscous components:

$$\mathbf{f}_j = \mathbf{f}_{j,c} - \mathbf{f}_{j,v} \tag{2}$$

where $\mathbf{f}_{j,c}$ is the convective flux and $\mathbf{f}_{j,v}$ is the viscous flux. Consider the control volume boundary that moves with the velocity $b_j = \frac{\partial x_j}{\partial t}$, the flux terms can now be written as

$$\mathbf{f}_{j,c} = \begin{bmatrix} \rho\,(u_j - b_j) \\ \rho u_1\,(u_j - b_j) + p\,\delta_{1j} \\ \rho u_2\,(u_j - b_j) + p\,\delta_{2j} \\ \rho u_3\,(u_j - b_j) + p\,\delta_{3j} \\ \rho E\,(u_j - b_j) + p\,u_j \end{bmatrix} \quad \text{and} \quad \mathbf{f}_{j,v} = \begin{bmatrix} 0 \\ \tau_{1j} \\ \tau_{2j} \\ \tau_{3j} \\ u_m \tau_{mj} - q_j \end{bmatrix} \tag{3}$$

where δ_{mj} is the Kronecker delta, q_j is the heat flux in the j direction and τ_{mj} is the stress tensor. Its components are given by

$$\tau_{mj} = \mu \left(\frac{\partial u_j}{\partial x_m} + \frac{\partial u_m}{\partial x_j} \right) + \delta_{mj} \lambda \frac{\partial u_l}{\partial x_l}$$

where μ is the dynamic viscosity of the fluid and λ is the second coefficient of viscosity, which is equal to $-\frac{2}{3}\mu$. The dynamic viscosity can be modeled using Sutherland's law where μ is a function of temperature:

$$\mu = \frac{\left(1.458 \times 10^{-6}\right) T^{\frac{3}{2}}}{T + 110.4}, \qquad T = \frac{p}{(\gamma - 1)\rho}.$$

With the aid of Fourier's law of heat conduction, the heat flux q_j is defined as

$$q_j = -k \frac{\partial T}{\partial x_j},$$

where k is the thermal conductivity of the fluid, which is defined as

$$k = \frac{\gamma \mu}{\mathrm{Pr}}.$$

The values of the ratio of specific heats, γ, and Prandtl number are held constant at 1.4 and 0.725 respectively. The equation of state provides the closure for the governing equations. For an ideal gas

$$E = \frac{p}{(\gamma - 1)\rho)} + \frac{1}{2}\left(u_j u_j\right), \qquad H = E + \frac{p}{\rho}.$$

For Euler calculation, the term $\mathbf{f}_{j,v}$ in Eq. (2) is set to zero.

Using central differencing with an artificial dissipation scheme for spatial discretization, the flow equations in Eq. (1), can be written in semi-discrete form:

$$\mathcal{V} \frac{\mathrm{d}\mathbf{w}}{\mathrm{d}t} + \mathbf{R}(\mathbf{w}) = 0. \tag{4}$$

III. Time Spectral Method

TAKING advantage of the periodic nature of the periodic unsteady problem, a Fourier representation in time can make it possible to achieve spectral accuracy. However, typical nonlinear frequency domain solvers require forward and backward Fourier transforms between the time and frequency domain for every time step. The Time Spectral method addresses this problem by utilizing the Fourier collocation matrix. As a result, the governing equations are now solved strictly in the time domain only.

Recall that for a real, periodic function, $f(x)$, defined on N equally spaced grid points, $x_j = j\Delta x$ where $j = 0, 1, 2, \ldots, N-1$. The discrete Fourier transform of f is

$$\hat{f}_k = \frac{1}{N} \sum_{j=0}^{N-1} f_j \mathrm{e}^{-\mathrm{i}kx_j}, \tag{5}$$

and its inverse transform is

$$f_j = \sum_{k=-\frac{N}{2}}^{\frac{N}{2}-1} \hat{f}_k \mathrm{e}^{\mathrm{i}kx_j}. \tag{6}$$

Then, the Fourier transform of the derivative approximation is computed by multiplying the Fourier transform of f by $\mathrm{i}k$

$$\widehat{Df_k} = \mathrm{i}k\hat{f}_k.$$

Therefore the spectral derivative of f at point j is

$$\left.\frac{\mathrm{d}f}{\mathrm{d}x}\right|_j = \sum_{k=-\frac{N}{2}+1}^{\frac{N}{2}-1} \widehat{Df_k} \mathrm{e}^{\mathrm{i}kx_j}.$$

Note that in the above representation, the period in space is 2π, and the Fourier coefficient of the derivative corresponding to the wave number $-N/2$ is set to zero to avoid complex derivatives.

If one wishes to have a compact representation of the spectral Fourier derivative operator in the physical space and not in the wave space, a physical (time) space operator for numerical differentiation can be derived for the governing equations as follows.

Using the definition from Eqs. (5) and (6), the discrete Fourier transform of the flow variables $\mathbf{w}$ for a time period T is

$$\widehat{\mathbf{w}}_k = \frac{1}{N} \sum_{n=0}^{N-1} \mathbf{w}^n \mathrm{e}^{-\mathrm{i}k\frac{2\pi}{T}n\Delta t},$$

and its inverse transform is

$$\mathbf{w}^n = \sum_{k=-\frac{N}{2}}^{\frac{N}{2}-1} \widehat{\mathbf{w}}_k \mathrm{e}^{\mathrm{i}k\frac{2\pi}{T}n\Delta t} \tag{7}$$

where $n\Delta t$ is the n-th time instance in the period T. The spectral derivative of Eq. (7) with respect to time at the n-th time stance is given by

$$D\mathbf{w}^n = \frac{2\pi}{T} \sum_{k=-\frac{N}{2}+1}^{\frac{N}{2}-1} \mathrm{i}k\, \widehat{\mathbf{w}}_k \mathrm{e}^{\mathrm{i}k\frac{2\pi}{T}n\Delta t}.$$

This summation involves the Fourier transform of $\mathbf{w}$ but it can be written as a matrix multiplication in the time domain as

$$D\mathbf{w}^n = \sum_{j=0}^{N-1} d_n^j \mathbf{w}^j$$

where

$$d_n^j = \begin{cases} \frac{2\pi}{T}\frac{1}{2}(-1)^{n-j} \cot\left\{\frac{\pi(n-j)}{N}\right\} & : \quad n \neq j \\ 0 & : \quad n = j \end{cases}.$$

This representation of the time derivative expresses the multiplication of a matrix (Canuto *et al.*, 2007)[5] with elements d_j^n and the vector $\mathbf{w}^j$.

Let $n - j = -m$, one can rewrite the time derivative as

$$D\mathbf{w}^n = \sum_{m=-\frac{N}{2}+1}^{\frac{N}{2}-1} d_m \mathbf{w}^{(n+m)}, \tag{8}$$

where d_m is now given by

$$d_m = \begin{cases} \frac{2\pi}{T}\frac{1}{2}(-1)^{m+1}\cot\left\{\frac{\pi m}{N}\right\} & : \quad m \neq 0 \\ 0 & : \quad m = 0 \end{cases}.$$

Substituting the spectral derivative of the flow variables in Eq. (8) into Eq. (4), the flow equations in semi-discrete form for the n-th time instance is

$$\mathcal{V} D\mathbf{w}^n + \mathbf{R}(\mathbf{w}^n) = 0. \tag{9}$$

These comprise a four dimensional coupled space–time set of nonlinear equations, which need to be solved simultaneously. For this purpose, we introduce a pseudo time derivative term to Eq. (9). The equations can now be marched towards a periodic steady state using well known convergence acceleration techniques

$$\mathcal{V}\frac{\mathrm{d}\mathbf{w}^n}{\mathrm{d}\tau} + \mathcal{V} D\mathbf{w}^n + \mathbf{R}(\mathbf{w}^n) = 0. \tag{10}$$

In order to solve Eq. (10) to the steady state as quickly as possible, the flow solver incorporated a number of convergence acceleration techniques; local time stepping, modified five stage Runge–Kutta time stepping scheme[6] and multigrid.[7,8] Two different artificial dissipation schemes were used; Jameson–Schmidt–Turkel[9] (JST) and convective upwind and split pressure[10] (CUSP).

For the RANS calculations of the forward flight, Message Passing Interface (MPI) were used between blocks. All the meshes used in this work were generated internally by the flow solvers. In the case of forward flight calculations, domain decomposition was done automatically.

IV. Vorticity Confinement for Compressible Flow

Steinhoff;[11] Steinhoff & Underhill[12] introduced the concept of Vorticity Confinement in 1994 and have been refining the model over the past decade. The basic idea of this method is to add a forcing term to the incompressible momentum equations, resulting in

$$\frac{\partial \mathbf{u}}{\partial t} + (\mathbf{u}\cdot\nabla)\,\mathbf{u} = -\frac{1}{\rho}\nabla p + \mu\nabla^2\mathbf{u} - \epsilon\mathbf{s} \tag{11}$$

where the simplest form of $\mathbf{s}$ is

$$\mathbf{s} = \hat{\mathbf{n}} \times \boldsymbol{\omega},$$

and

$$\hat{\mathbf{n}} = \frac{\nabla\boldsymbol{\eta}}{|\nabla\boldsymbol{\eta}|}.$$

The vorticity vector $\boldsymbol{\omega}$ given by

$$\boldsymbol{\omega} = \nabla \times \mathbf{u}.$$

The variable $\boldsymbol{\eta}$ is defined as

$$\boldsymbol{\eta} = |\boldsymbol{\omega}|\,.$$

The idea behind this formulation is that vorticity is convected in the direction determined by the gradients of the vorticity. The unit vector $\hat{\mathbf{n}}$ points towards the core of the vortical region and the confinement term $\mathbf{s}$ convects the vorticity towards the centroid.

The authors combine the previous works of Hu *et al.*;[13] Hu & Grossman,[14] Fedkiw *et al.*;[15] Löhner & Yang;[16] Löhner *et al.*[17] and Robinson,[18] to obtain an alternative formula which can be written as follows:[1]

$$\mathbf{s} = |\mathbf{u}\cdot\boldsymbol{\omega}|\left[1+\log_{10}\left(1+\frac{\mathcal{V}}{\mathcal{V}_{\text{averaged}}}\right)^{1/3}\right]\begin{bmatrix} 0 \\ \rho\left(\hat{\mathbf{n}}\times\frac{\boldsymbol{\omega}}{|\boldsymbol{\omega}|}\right)\cdot\mathbf{i} \\ \rho\left(\hat{\mathbf{n}}\times\frac{\boldsymbol{\omega}}{|\boldsymbol{\omega}|}\right)\cdot\mathbf{j} \\ \rho\left(\hat{\mathbf{n}}\times\frac{\boldsymbol{\omega}}{|\boldsymbol{\omega}|}\right)\cdot\mathbf{k} \\ \rho\left(\hat{\mathbf{n}}\times\frac{\boldsymbol{\omega}}{|\boldsymbol{\omega}|}\right)\cdot\mathbf{u} \end{bmatrix}. \tag{12}$$

V. Forward Flight Simulations

In forward flight regime, a component of free stream velocity U_0 adds or subtracts from the rotational velocity at each part of the blade. So the tip velocity U_{tip} now becomes

$$U_{\text{tip}} = \Omega R + U_0 \sin\psi$$

where ψ is the azimuthal angle of the blade. ψ is defined as zero in the downstream direction of the rotor. This angle is measured from downstream to the blade span axis.

Although the rotor blade is normally twisted along its length (linear twist), the blades in the current work are rigid and do not account for aeroelastic effects. Results are compared to the wind tunnel experiment of a model helicopter rotor in forward flight by Caradonna *et al.*[19] The blades were 7 feet in diameter and 6 inches in chord with an untapered, untwisted NACA 0012 profile.

V.A. Mesh

The mesh for nonlifting forward flight calculations is an O–H type mesh that is internally generated via conformal mapping. Fig. 1 shows the mesh used in the calculations.

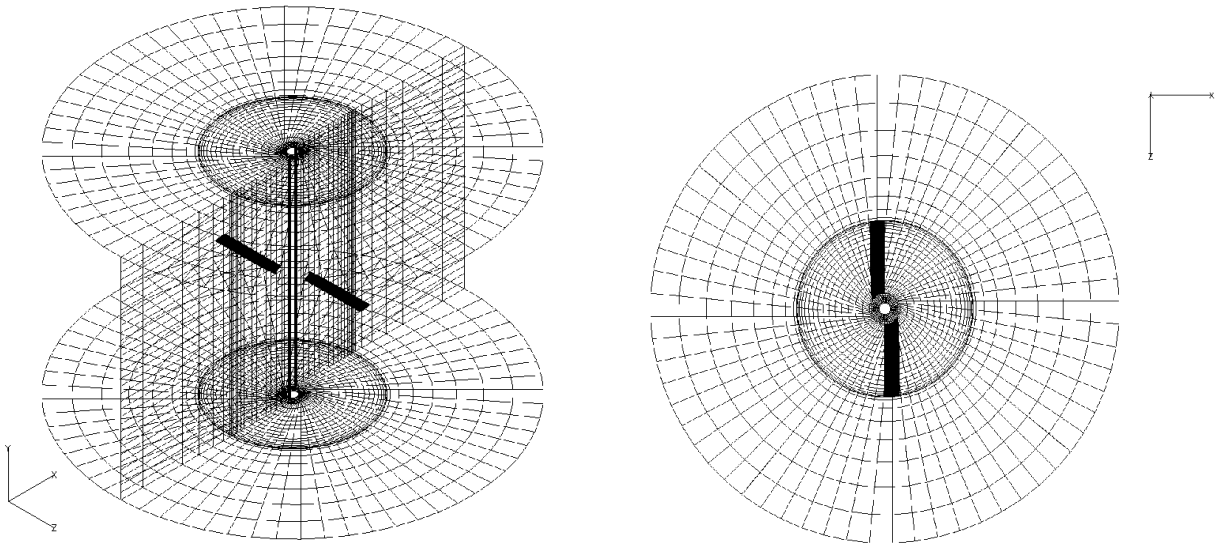

(a) Isometric view (b) Top view

Figure 1. $128 \times 48 \times 32$ computational mesh cells per blade modeling an untwisted, untapered, two-bladed NACA 0012 rotor with an aspect ratio of 7 for the Euler calculation of a rotor in nonlifting forward flight

V.B. Boundary Conditions

At the rotor hub, a solid body boundary (flow tangency for Euler calculation and no slip for RANS calculation) condition was used. Reimann invariants boundary condition was also tested but the overall result was insensitive to the boundary condition at this boundary.

At the far-field, the boundary condition was constructed using one-dimensional Reimann invariants for both the upper and lower boundaries. The halo cells at the side boundaries containing both the values of the flow variables, mesh geometry and mesh velocities were exchanged between the blades at every time step.

V.C. Nonlifting Rotor in Forward Flight

The aspect ratio of the blades was 7. The tip Mach number was 0.8 with the reference Reynolds number of 2.89×10^6. The advance ratio was $\mu = 0.2$, which corresponded to a Mach number in the unperturbed flow of $M_0 = 0.16$.

For the Euler calculations, the number of cells per blade was $128 \times 48 \times 32$ with 16 cells distributed along the blade while $192 \times 64 \times 48$ cells were used for the RANS calculations with 32 cells distributed along each blade. All the calculations were performed with 12 time instances ($N = 12$), or five harmonics.

Fig. 2 shows the variation of the local coefficient of pressure at the span location $r/R = 0.893$ for six different azimuthal angles. The results were from the Euler calculations with the JST and CUSP dissipation schemes. The agreement between the computed results and the experimental data was very good. The shock captured using the CUSP dissipation scheme was sharper and stronger, and is most obvious at the azimuthal angle $\psi = 120°$. The shock location calculated with both artificial dissipation schemes was almost the same, and this occurred earlier than the shock location recorded in the experiment. The Euler calculations took 300 multigrid cycles, by which time, the averaged residual was reduced by more than four orders of magnitude.

Fig. 3 shows the result of the RANS calculations with the JST and CUSP dissipation schemes. Similarly, the calculations show excellent agreement with the experimental data. The result from the CUSP scheme showed slightly weaker shock in this calculation than in the corresponding Euler calculations. This was expected because of the viscous effects. The RANS computations with 12 time instances were run on four dual-core processors with the clock speed of 3.0 GHz. The total simulation time including mesh generation, which was built into the flow solver, was five hours for 500 multigrid cycles with three orders of magnitude reduction in the averaged residual.

V.D. Accuracy Tests

As an accuracy test of the Time Spectral method, the forward flight case was simulated with only four time instances ($N = 4$). Results from Euler calculations at the azimuthal angles $\psi = 90°$ and $\psi = 180°$ are shown in Fig. 4. One can observe that even with a small number of time instances, as few as only four, the results still show excellent agreement with the experimental data. This shows that the Time Spectral method is indeed, a highly accurate scheme while avoids being computationally expensive.

V.E. Cost Comparison

As a comparison to the traditional backward difference formula,[3] a RANS calculation of a rotor in forward flight for the same case would require the following operations at the minimum:

- 180 time steps per revolution (more likely 360 time steps, if not more).
- 40 multigrid cycles per time step.
- 6 complete cycles to establish periodicity of the flow field.

This means at least 43,200 cycles would be required to solve the same problem, whereas the calculation with the Time Spectral method used only 500 multigrid cycles. Therefore the Time Spectral method is at least two orders of magnitude faster than the backward difference formula. Even when one considers that 12 time instances are used for one calculation, the computational resource required is still approximately 10 times less than calculations with BDF.

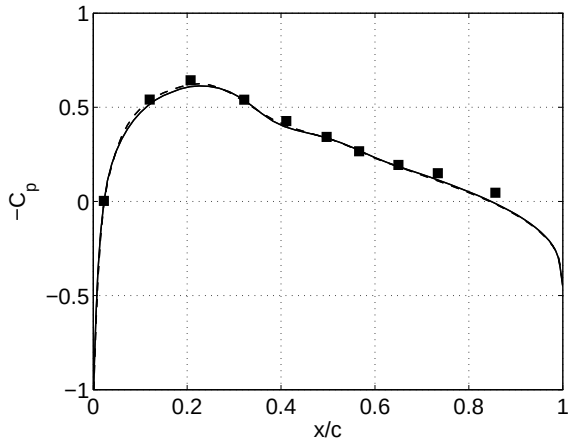

(a) C_p distribution at $\psi = 30°$

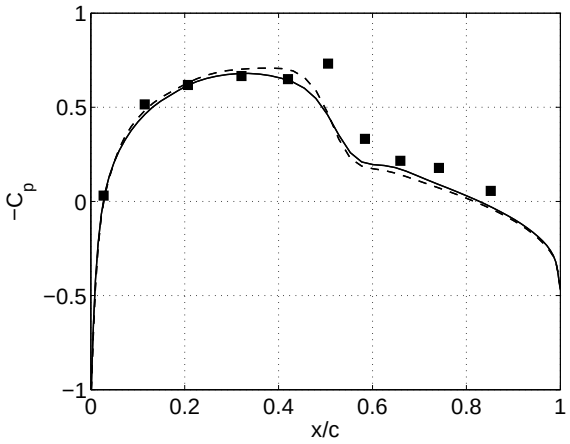

(b) C_p distribution at $\psi = 60°$

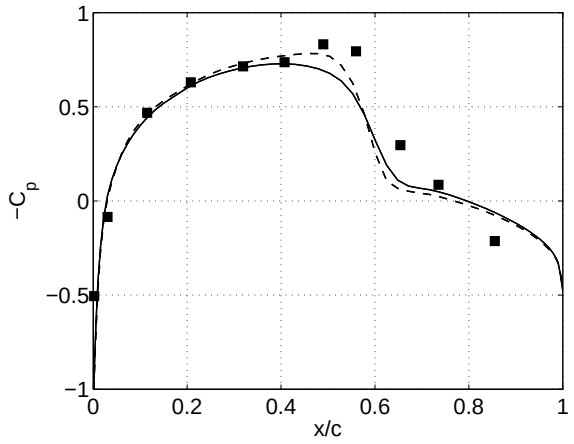

(c) C_p distribution at $\psi = 90°$

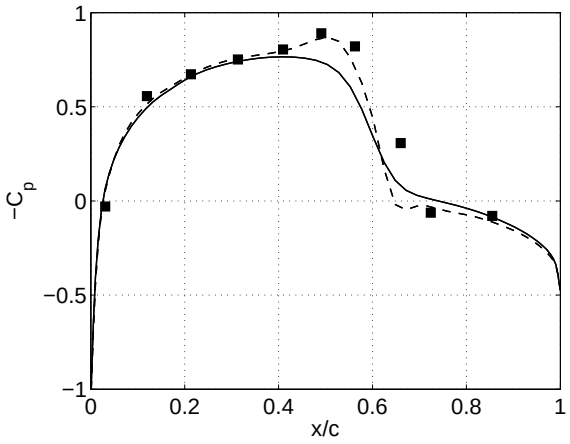

(d) C_p distribution at $\psi = 120°$

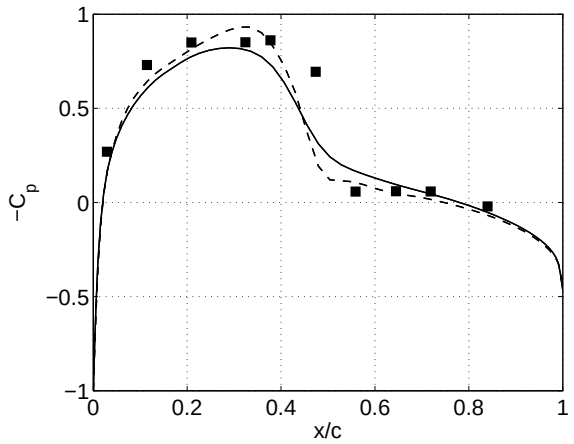

(e) C_p distribution at $\psi = 150°$

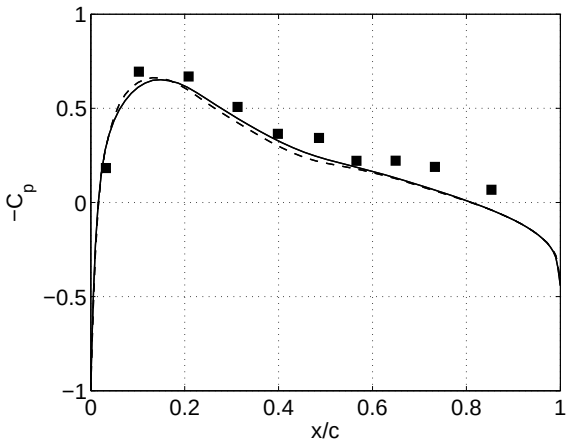

(f) C_p distribution at $\psi = 180°$

Figure 2. Coefficient of pressure distribution on a blade section at $r/R = 0.893$ on a nonlifting rotor in forward flight from Euler calculations, $\mathbf{M_{tip} = 0.8}$, $\theta_c = 0°$, $\mu = 0.2$, $N = 12$: ■ denotes the experimental values of C_p, — denotes the result using the JST dissipation scheme, and − − denotes the result using the CUSP dissipation scheme.

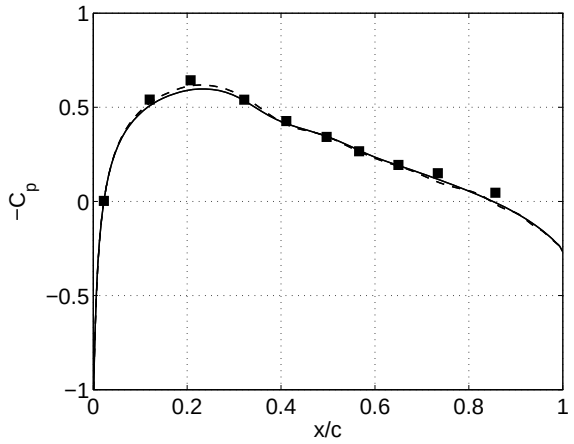

(a) C_p distribution at $\psi = 30°$

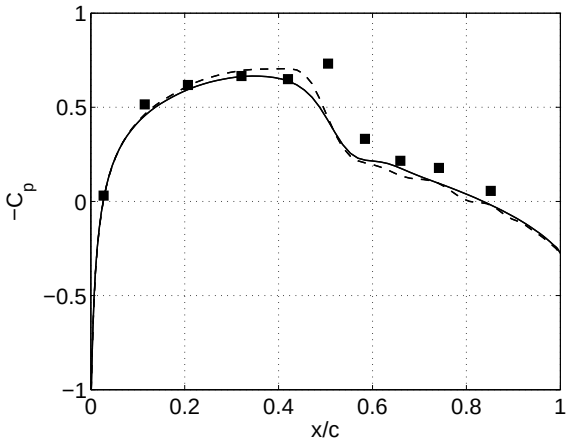

(b) C_p distribution at $\psi = 60°$

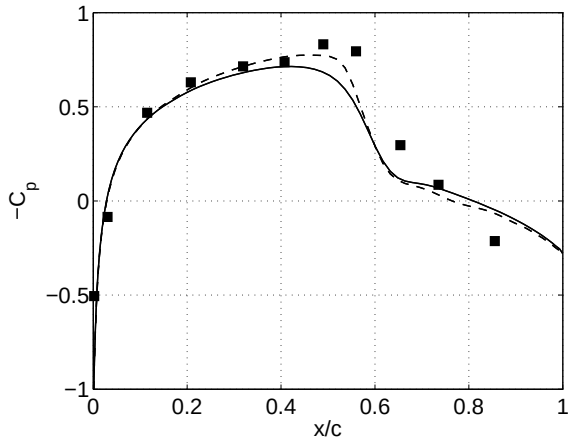

(c) C_p distribution at $\psi = 90°$

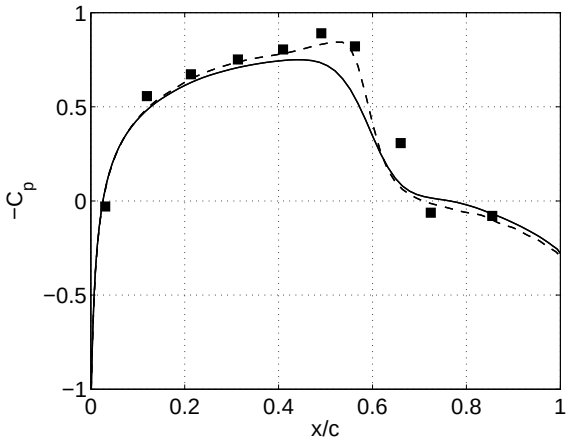

(d) C_p distribution at $\psi = 120°$

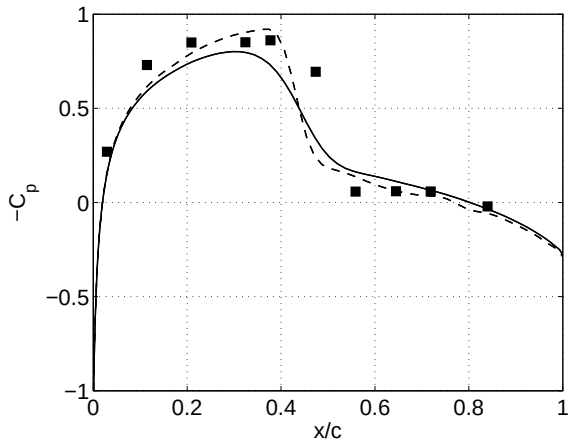

(e) C_p distribution at $\psi = 150°$

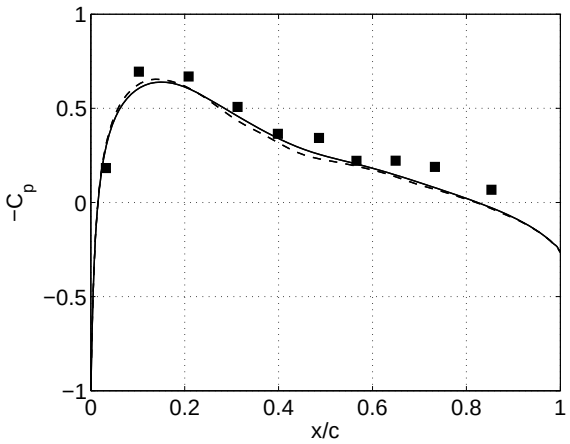

(f) C_p distribution at $\psi = 180°$

Figure 3. Coefficient of pressure distribution on a blade section at $r/R = 0.893$ on a nonlifting rotor in forward flight from RANS calculations, $\mathbf{M_{tip} = 0.8}$, $\theta_c = 0°$, $\mu = 0.2$, $N = 12$: ■ denotes the experimental values of C_p, — denotes the result using the JST dissipation scheme, and − − denotes the result using the CUSP dissipation scheme.

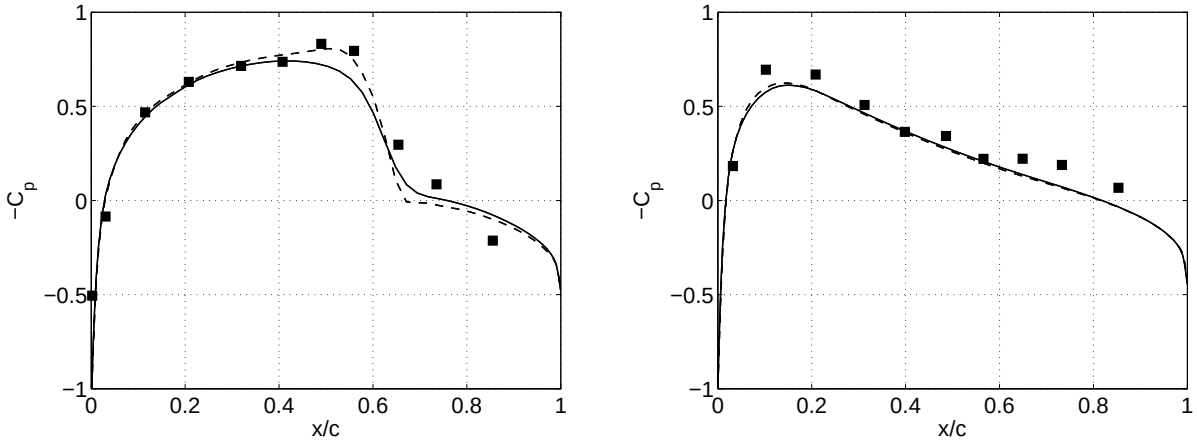

(a) C_p distribution at $\psi = 90°$

(b) C_p distribution at $\psi = 180°$

Figure 4. Coefficient of pressure distribution on a blade section at $r/R = 0.893$ on a nonlifting rotor in forward flight from Euler calculations, $N = 4$, $\mathbf{M_{tip} = 0.8}$, $\theta_c = 0°$, $\mu = 0.2$: ■ denotes the experimental values of C_p, — denotes the result using the JST dissipation scheme, and − − denotes the result using the CUSP dissipation scheme.

V.F. Lifting Rotor in Forward Flight

In this section, calculation results for a lifting rotor in forward flight is compared to the numerical simulation of Professor Chris Allen of the University of Bristol. The geometry for this test case is the same as the lifting hover case.[20] The aspect ratio is six with an NACA 0012 blade section, and the collective pitch is 8 degrees. The tip Mach number is set at 0.7 and the advance ratio, μ, is 0.2857. This corresponds to a forward flight Mach number of 0.2.

This test case has been chosen for a number of reasons. The primary reason is that there is no blade motion, i.e. the blades are completely rigid with no allowance for aeroelasticity effects and the rotor hub is not articulated. Additionally, simulations by Allen[21] used 4 million mesh points with 60 time steps per revolution, and 70 four-level V-cycle multigrid inner iterations for each time step. The time integration for this work was the widely used BDF.[3] Thus Allen's results seem accurate enough for comparison purposes. His past work has been thorough and he has consistently obtained good agreement between his numerical results and the experimental data. Lastly, the number of mesh cells used in the current work is approximately 200,000 per blade sector for the smallest case. While this relatively small number of mesh cells may not be able to fully resolve all details of the correct flow field, the results indicate that the prediction of aerodynamic quantities such as the coefficient of pressure, is remarkably accurate for the mesh size.

The quantity compared here is the load variation on each blade around the azimuth. Allen defined the force coefficient for each blade as

$$C_L = \frac{F_y}{\frac{1}{2}\rho\left(\Omega R\right)^2 cR} \tag{13}$$

where c is the chord at the tip (the chord is constant along the radius in this case), F_y is the force in the y direction, Ω is the angular velocity and the term cR represents the surface area of the blade. The subscript L indicates the lifting load. It is different from the coefficient of thrust in that this quantity is only for one blade, not for the complete rotor as one would associate with the thrust. Figures 5 and 6 show the comparison of the load variation computed by the Time Spectral method with the JST and CUSP dissipation schemes, and the data that has been supplied by Professor Allen.

Only one sector of a rotor is used in this calculation using the time-lagged periodic boundary condition from (**??**). Four cases for each scheme are compared with different combinations of the number of mesh cells and time instances. The cases are summarized in table 1. The number of time instances used in the calculations are 12 for cases 1–3 and 18 for case 4 as indicated in the table. This corresponds to azimuthal angles of 0, 30, 60, . . . , 330, 360 degrees for the first case, and 0, 20, 40, . . ., 340 and 360 degrees for the second case. Periodicity was not established in Allen's result until the second revolution. The computed

result is thus shifted by 360°. Additionally, 90° is added because of the difference in the rotor orientation. Therefore the comparison starts at $\psi = 450°$ onwards.

The comparison of the first three cases can be thought of as a mesh refinement study, although this should be done by doubling the number of mesh points in all directions, rather than increasing the number of points by small numbers as it is shown here. All three cases over-predict the lift coefficient except around the azimuthal angle greater than 90° and less than 225° approximately. This is not unexpected since the blade geometry from the Caradonna–Tung experiment was not fully specified such as where the root of the blade actually starts (only the diameter of the rotor and the aspect ratio are given). Different researchers presumably use slightly different geometries in this regard. The calculation with 18 time instances shows better agreement of the lift coefficient on the retreating side for both dissipation schemes, but the over-prediction of the lift coefficient between azimuthal angles of 0° and 30° is greater than the calculations with 12 time instances.

Allen explained that there was a dip in the coefficient of lift, C_L, around an azimuth angle approximately between 0° and 30° because the blade was running into the vortex generated from the previous blade. In the present work, it is not very visible that there is a dip in the lift coefficient in this area with the result from the JST scheme. This phenomenon is more visible with the CUSP dissipation scheme. It can be observed that as the number of mesh size increases, this feature starts to look more prominent.

Case	Number of Cells			Number of Time Instances
	x	y	z	N
1	128	48	32	12
2	160	48	48	12
3	192	64	48	12
4	160	48	48	18

Table 1. Lifting forward flight test conditions.

Figures 7 and 8 show the distribution of the coefficient of pressure at $r/R = 0.90$ at 12 azimuthal angles from calculations with the JST and CUSP dissipation schemes. This corresponds to case 3 in the table. The calculations used $192 \times 64 \times 48$ mesh cells. The span $r/R = 0.90$ is chosen for comparison because discontinuity is certain to appear in the advancing side near the tip. A good agreement with the data provided by Allen is observed except at three azimuthal angles, 150°, 180° and 330°. Personal consultation with Professor Allen suggested that the number of mesh points is not enough to capture shock at the first two locations. The coefficient of pressure distribution at 330° over-predicts the result of Allen's by some margin. However, this location is on the retreating side and there is no physical reason why the coefficient of pressure should significantly drop only to rise up again at 360°.

VI. Computed Results with Vorticity Confinement

THE test case was a fully compressible Euler computation of wing tip vortex of a NACA 0012 wing with an aspect ratio of 3. The free stream Mach number was 0.8 and the angle of attack was 5 degrees. At $z = 0$, a symmetry plane boundary condition was used. Riemann invariants boundary condition was applied at the far-field and a flow tangency boundary condition was used on the wing. The formulation of the Vorticity Confinement method was taken from Eq. (12). Calculations were performed with four different values of the confinement parameter ϵ.

The mesh was generated internally by the flow solver and was a typical C-mesh type with $160 \times 32 \times 48$ mesh cells with 32 cells on the wing. The reference chord length was unity and the trailing edge was located at $x = 1$. The coefficient ϵ was fixed at 0, 0.025, 0.05, and 0.075. The results from the calculations are shown in Fig. 9. There are four cut-planes normal to the x direction located at $x = 2, 4, 6$, and 8, where the vorticity magnitude was plotted. One can observe that the vortex structure was still quite well maintained even after eight chord lengths away with the confinement term. The effectiveness of this depended on the strength of the confinement parameter. For the case of no confinement $\epsilon = 0$, the vorticity dissipated very quickly.

Fig. 10 shows the distribution of the coefficient of pressure on the wing at three different span stations.

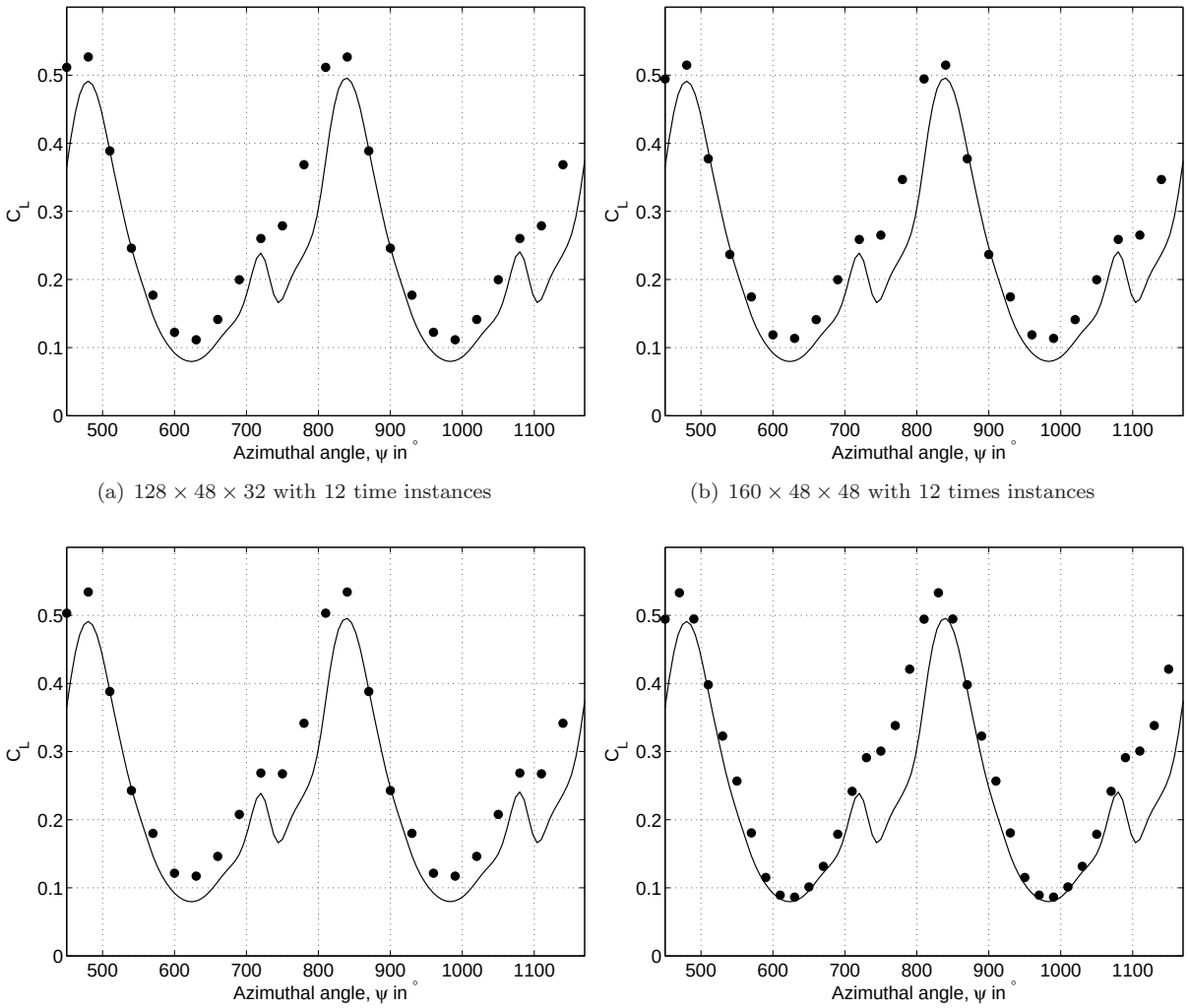

(a) $128 \times 48 \times 32$ with 12 time instances

(b) $160 \times 48 \times 48$ with 12 times instances

(c) $192 \times 64 \times 48$ with 12 time instances

(d) $160 \times 48 \times 48$ with 18 time instances

Figure 5. Comparison of the coefficient of lift per blade vs. the azimuth of a lifting rotor in forward flight from Euler calculation with the CUSP dissipation scheme, $M_t = 0.7$, $\mu = 0.2857$, $\theta_c = 8^\circ$: • computed result from the current work using the JST dissipation scheme, — simulation result provided by Allen.

	$z = 0.891$		$z = 1.828$		$z = 2.766$	
ϵ	c_l	c_d	c_l	c_d	c_l	c_d
0	0.7098	0.0792	0.6123	0.0651	0.3869	0.0394
0.025	0.7091	0.0791	0.6114	0.0650	0.3851	0.0393
0.050	0.7083	0.0790	0.6103	0.0649	0.3833	0.0391
0.075	0.7074	0.0788	0.6093	0.0647	0.3817	0.0389

Table 2. Coefficients of lift and drag from Euler calculation of a NACA 0012 wing for different values of ϵ at three different span stations: $M_\infty = 0.8$, $\alpha = 5$, aspect ratio = 3.

The effect of adding the confinement term was negligible and the distribution of the coefficient of pressure for each value of ϵ collapsed into one line. The coefficients of lift and drag at three different span stations are listed in Table 2 and are plotted separately in Fig. 11. The coefficients of lift and drag decreased by approximately 0.3% and 0.5% respectively as the confinement parameter ϵ increased from zero to 0.075 at

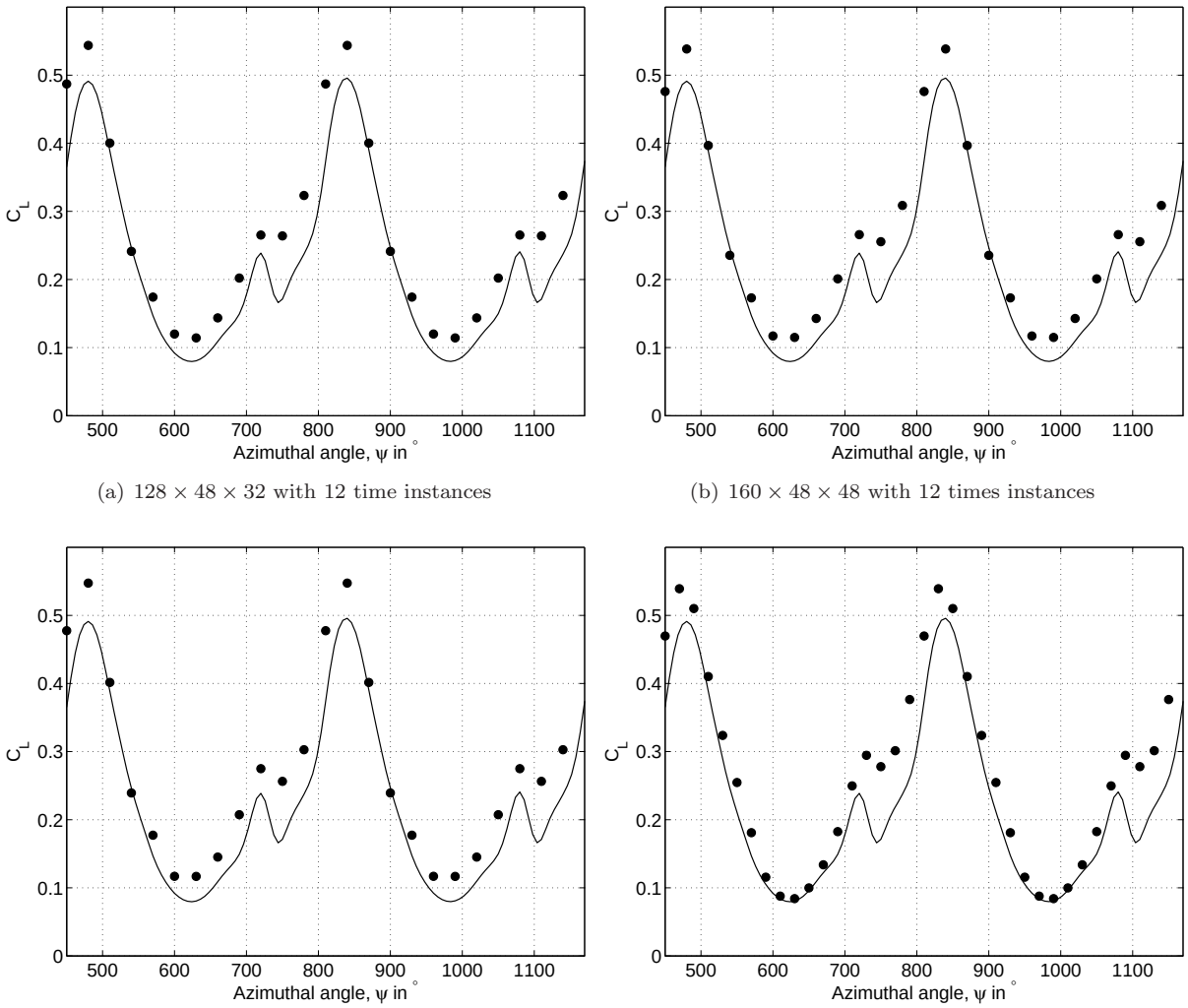

(a) $128 \times 48 \times 32$ with 12 time instances

(b) $160 \times 48 \times 48$ with 12 times instances

(c) $192 \times 64 \times 48$ with 12 times instances

(d) $160 \times 48 \times 48$ with 18 time instances

Figure 6. Comparison of the coefficient of lift per blade vs. the azimuth of a lifting rotor in forward flight from Euler calculation with the CUSP dissipation scheme, $M_t = 0.7$, $\mu = 0.2857$, $\theta_c = 8^\circ$: • computed result from the current work using the CUSP dissipation scheme, — simulation result provided by Allen.

$z = 0.891$, and up to 1.3% for both coefficients at $z = 2.766$. The location $z = 2.766$ was very close to the tip of the wing ($z_{\text{tip}} = 3$), and this was where the tip vortex was generated. Therefore the difference in both c_l and c_d for different values of the confinement parameter was expected to be the largest at this location. The results from this test case indicate that the new formulation works well for transonic flow calculation and that the inclusion of the confinement term does not diminish the ability of the flow solver to capture discontinuity. The implementation of the new formulation of Vorticity Confinement is currently under investigation for rotorcraft flow.

VII. Vorticity Confinement in Rotorcraft Flow

This section discusses the application of Vorticity Confinement to rotorcraft simulation. A comparison is made with the data for a lifting rotor in forward flight supplied by Professor Allen. The geometry for this case is from[20] with a collective pitch of 8 degrees. The tip Mach number is 0.7 and the advance ratio is $\mu = 0.2857$. The computation used 12 time instances for Euler calculation with $160 \times 48 \times 48$ mesh cells. The formulation of Vorticity Confinement is from (12). Fig. 12 shows a significant improvement over the results

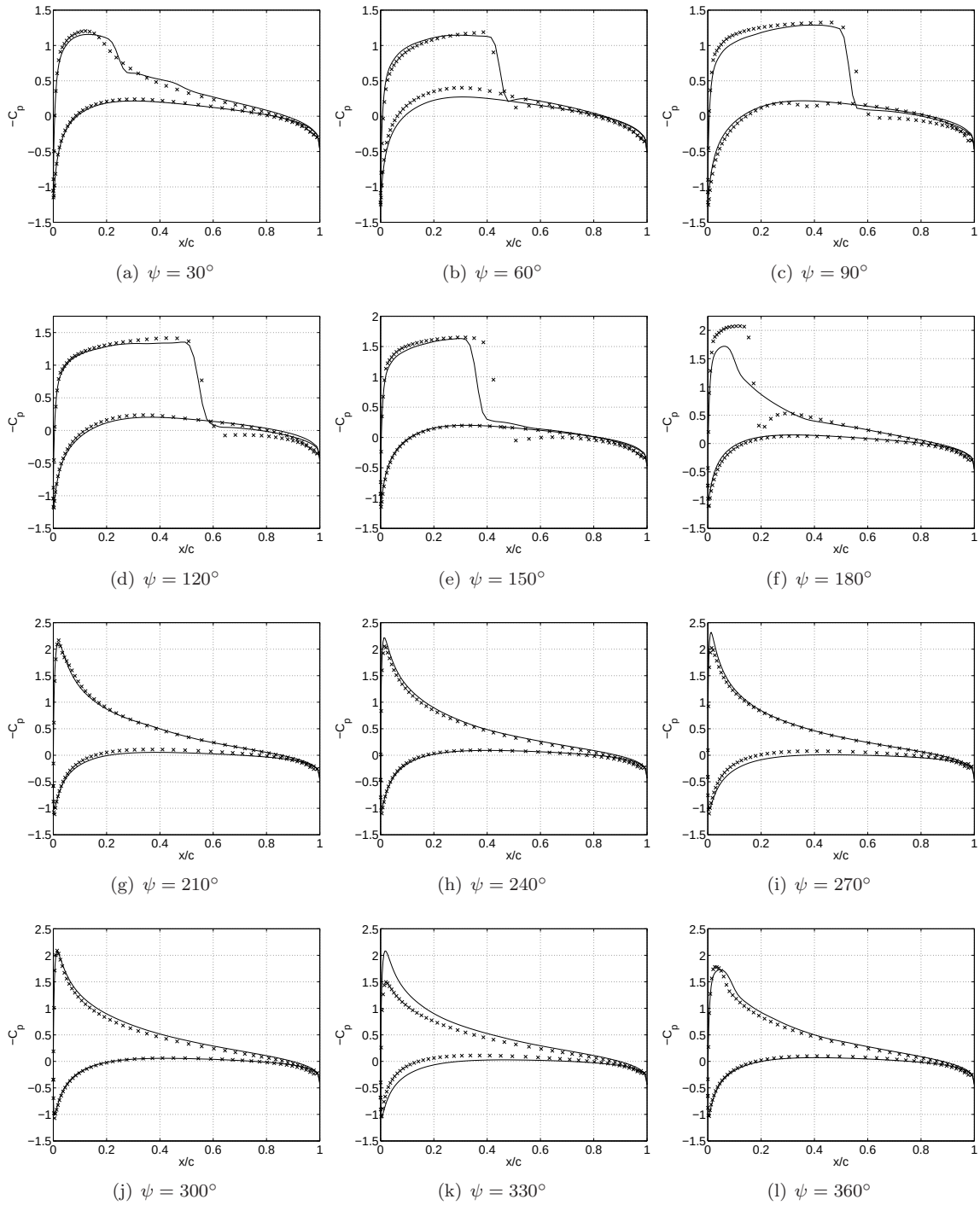

(a) $\psi = 30°$ (b) $\psi = 60°$ (c) $\psi = 90°$

(d) $\psi = 120°$ (e) $\psi = 150°$ (f) $\psi = 180°$

(g) $\psi = 210°$ (h) $\psi = 240°$ (i) $\psi = 270°$

(j) $\psi = 300°$ (k) $\psi = 330°$ (l) $\psi = 360°$

Figure 7. Coefficient of pressure at $r/R = 0.90$ using the JST dissipation scheme with $192 \times 64 \times 48$ mesh cells, $M_t = 0.7$, $\mu = 0.2857$, $\theta_c = 8°$, $N = 12$: — computed result, $\times$ result provided by Allen.

previously shown in figure 5. The over-prediction of the lift coefficient has decreased markedly, especially on the advancing side. As ϵ increases, one can easily observe the effects of the blade–vortex interaction at the beginning of the advancing side. Recall that the results from the JST scheme hardly exhibit the dip in the coefficient of lift, even at the largest mesh size of $192 \times 64 \times 48$. The results shown here used fewer mesh cells but the effect of the blade–vortex interaction can be seen clearly when the confinement parameter ϵ is

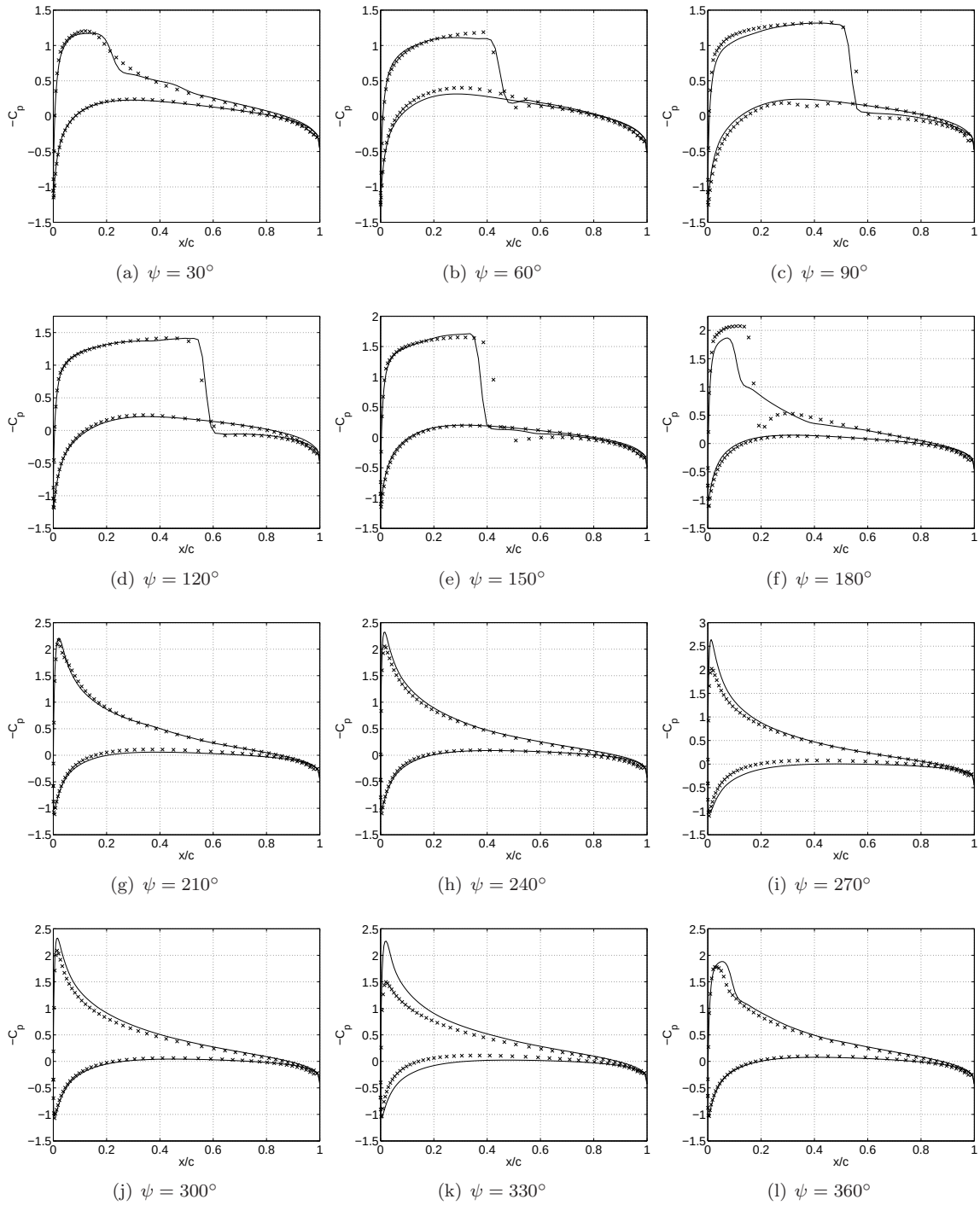

(a) $\psi = 30°$ (b) $\psi = 60°$ (c) $\psi = 90°$

(d) $\psi = 120°$ (e) $\psi = 150°$ (f) $\psi = 180°$

(g) $\psi = 210°$ (h) $\psi = 240°$ (i) $\psi = 270°$

(j) $\psi = 300°$ (k) $\psi = 330°$ (l) $\psi = 360°$

Figure 8. Coefficient of pressure at $r/R = 0.90$ using the CUSP dissipation scheme with $192 \times 64 \times 48$ mesh cells, $\mathbf{M}_t = 0.7$, $\mu = 0.2857$, $\theta_c = 8°$, $N = 12$: — computed result, $\times$ result provided by Allen.

sufficiently large.

The required value of the confinement parameter for this case is one order of magnitude larger than the fixed-wing case. This is because the skewed geometry of the helicopter mesh. Additionally, because the mesh cells are extremely small near the hub, confinement is only added in the outer half of the blade. The smallest mesh size for this case is of the order $\mathcal{O}(10^{-8})$ while the largest mesh cell is of the order of $\mathcal{O}(10^{-1})$.

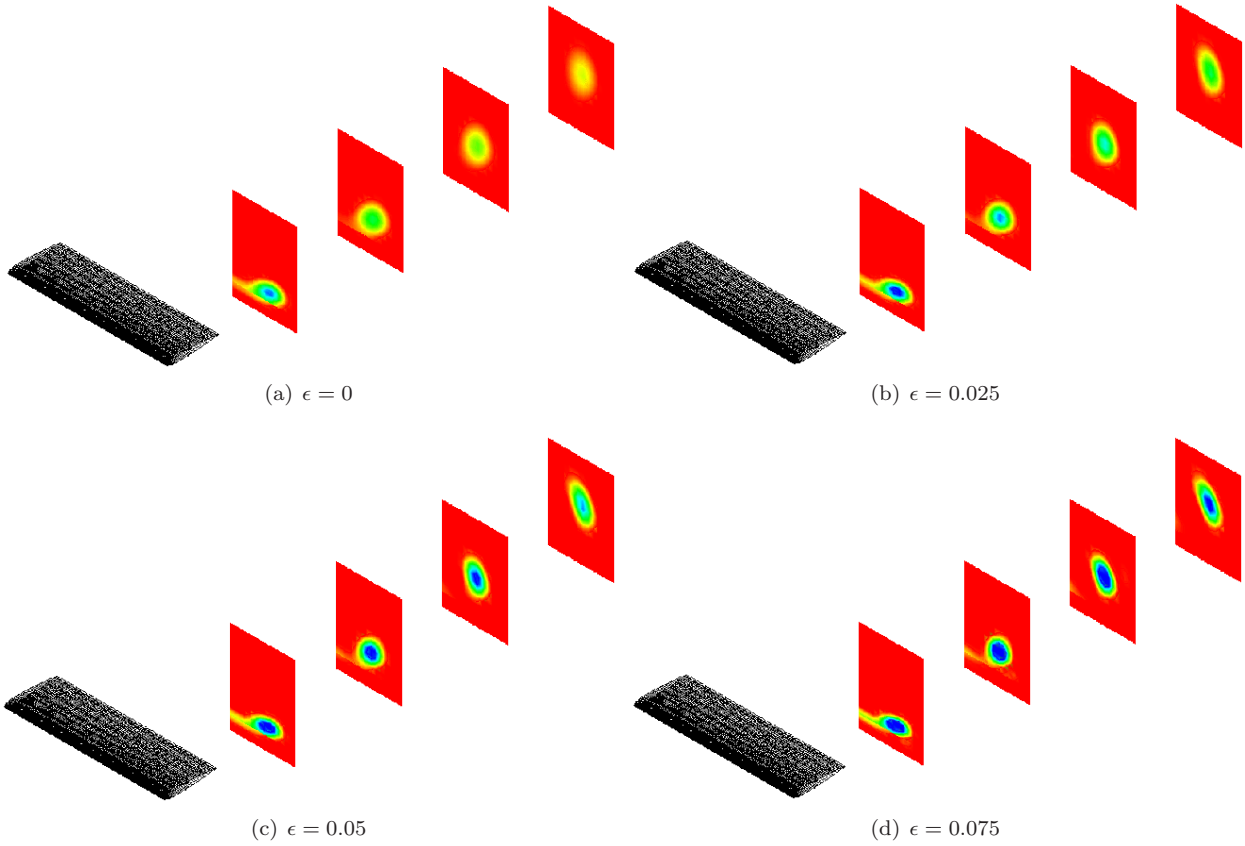

(a) $\epsilon = 0$ (b) $\epsilon = 0.025$

(c) $\epsilon = 0.05$ (d) $\epsilon = 0.075$

Figure 9. Vorticity magnitude on NACA 0012 wing for different values of ϵ: $M_\infty = 0.8$, $\alpha = 5$, aspect ratio = 3.

Fig. 13 shows the vorticity magnitude at the first time instance where $\psi = 90°$ at 2 cut-planes normal to the x direction where $x = 2$ and $x = 5$. The leading edge and the trailing edge are located at $x = 0$ and $x = 1$ respectively. It can be observed from the plots that the vortical structure could be maintained better with Vorticity Confinement compared to the result from the original calculation. However, the vortex structure still diffuses much faster compared to the results of the fixed-wing because the mesh distribution in the vortical regions is more sparse than the traditional C-mesh distribution. It is safe to assume that changing the current O–H mesh topology to an H–H mesh, or an unstructured mesh distribution should improve this matter significantly. The severity of the mesh stretching can be seen Fig. 14.

VIII. Summary & Conclusion

It has been shown that the Time Spectral method is capable of accurately predicting the helicopter aerodynamics. If one considers the number of multigrid cycles required to march to convergence, the Time Spectral method is at least two orders of magnitude cheaper than the traditional implicit dual time stepping scheme. Additionally, the method is simpler to implement compared to the nonlinear frequency domain technique.

The new formulation of the Vorticity Confinement method needs further investigation and validation before becoming robust enough for rotorcraft flow computation but the new formulation looks promising as it has no effect on the surface pressure distribution and only up to 1.3% error in the values of the coefficients of lift and drag. The parameter ϵ is now a true dimensionless parameter and the calculation of a helicity reflects the direction of the vortical structures of the rotorcraft flow field.

However, one issue that arises with Vorticity Confinement is that the confinement term is independent of the numerical schemes used in calculations. Since it is used to counteract the effect of numerical diffusion, the best value of the confinement parameter may vary when different numerical schemes are used, and is

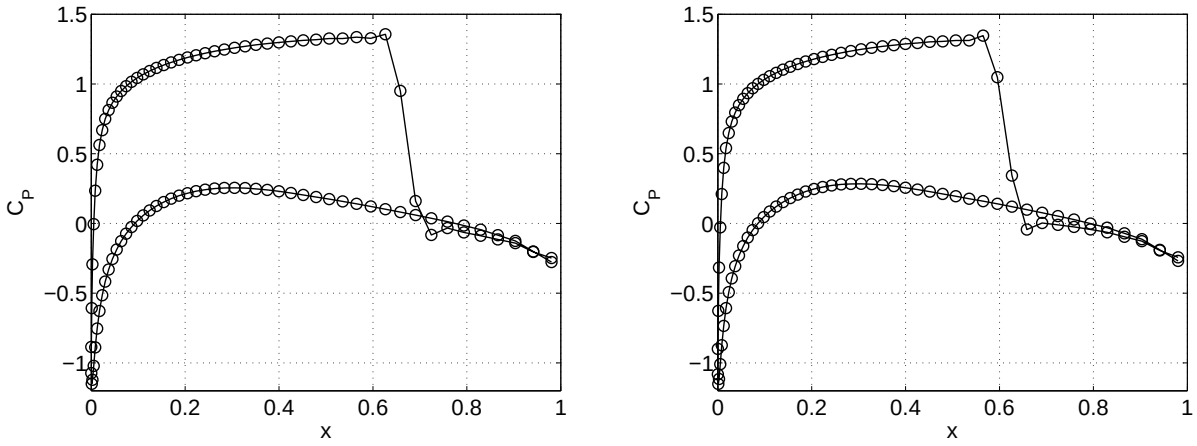

(a) Span station $z = 0.891$

(b) Span station $z = 1.828$

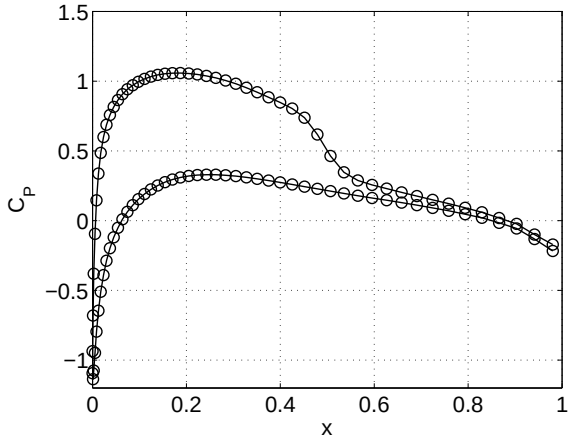

(c) Span station $z = 2.766$

Figure 10. Coefficient of pressure distribution at three span stations on NACA 0012 wing for four different values of ϵ: — ∘ — denotes $\epsilon = 0$, $\cdots$ denotes $\epsilon = 0.025$, $- \cdot -$ denotes $\epsilon = 0.05$, $- -$ denotes $\epsilon = 0.075$, $\mathbf{M}_\infty = 0.8$, $\alpha = 5$, aspect ratio = 3.

one of the major problems in correctly identifying the confinement parameter ϵ. Naturally, when one uses a high order scheme (higher than second order), numerical diffusion is considerably less in comparison to first or second order accurate schemes. As a result, there is a need to systematically formulate the confinement term based on numerical diffusion and discretization errors. The values used in this work for both fixed-wing and rotary-wing calculations have come from trial and error.

References

[1]Butsuntorn, N. and Jameson, A., "Time Spectral Method for Rotorcraft Flow"," *AIAA 46th Aerospace Sciences Meeting & Exhibit*, Reno, NV, January 2008, AIAA Paper 2008–0403.

[2]Gopinath, A. K. and Jameson, A., "Time Spectral Method for Periodic Unsteady Computations over Two- and Three-Dimensional Bodies," *AIAA 43th Aerospace Sciences Meeting & Exhibit*, Reno, NV, January 2005, AIAA Paper 2005–1220.

[3]Jameson, A., "Time Dependent Calculations Using Multigrid, with Applications to Unsteady Flows Past Airfoils and Wings," *AIAA 10th Computational Fluid Dynamics Conference*, Honolulu, HI, July 1991, AIAA Paper 1991–1596.

[4]Ekici, K., Hall, K. C., and Dowell, E. H., "Computationally Fast Harmonic Balance Methods for Unsteady Aerodynamic Predictions of Helicopter Rotors," *AIAA 46th Aerospace Sciences Meeting & Exhibit*, Reno, NV, January 2008, AIAA Paper 2008–1439.

[5]Canuto, C., Hussaini, M. Y., Quarteroni, A., and Zang, T. A., *Spectral Methods: Evolution to Complex Geometries and*

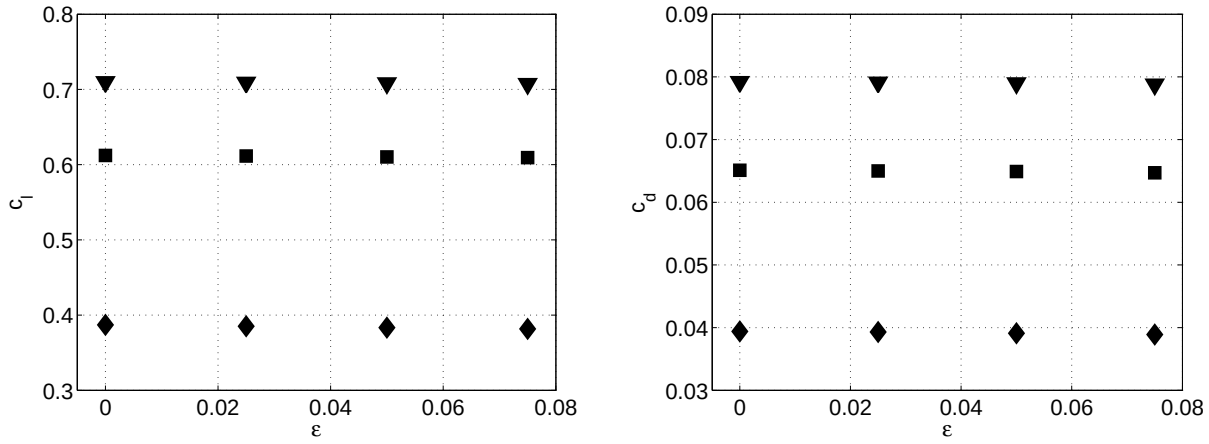

(a) Section c_l (b) Section c_d

Figure 11. Coefficients of lift and drag at three span stations from Euler calculation of a NACA 0012 wing for four different values of ϵ: ▼ at the span station $z = 0.891$, ■ at the span station $z = 1.828$, ♦ at the span station $z = 2.766$, $\mathbf{M}_\infty = 0.8$, $\alpha = 5$, aspect ratio = 3.

Applications to Fluid Dynamics, Springer–Verlag New York, LLC, 1st ed., September 2007.

[6]Jameson, A., *Numerical Methods in Fluid Dynamics*, Vol. 1127/1985 of *Lecture Notes in Mathematics*, chap. Transonic Flow Calculations, Springer Berlin/Heidelberg, 1985, pp. 156–242, Princeton University MAE Report 1651, March 1984.

[7]Jameson, A., "Solution of the Euler Equations For Two Dimensional Transonic by a Multigrid Method," *Applied Mathematics and Computation*, Vol. 13, 1983, pp. 327–356.

[8]Jameson, A., *Multigrid Methods II*, Vol. 1228 of *Lecture Notes in Mathematics*, chap. Multigrid Algorithms for Compressible Flow Calculations, Springer Berlin/Heidelberg, 1986, pp. 166–201, Proceedings of the 2nd European Conference on Multigrid Methods, Cologne, October 1985.

[9]Jameson, A., Schmidt, W., and Turkel, E., "Numerical Solutions of the Euler Equations by Finite Volume Methods Using Runge–Kutta Time-Stepping Schemes," *AIAA 14th Fluid and Plasma Conference*, Palo Alto, CA, June 1981, AIAA Paper 1981–1259.

[10]Jameson, A., "Analysis and Design of Numerical Schemes for Gas Dynamics 2: Artificial Diffusion and Discrete Shock Structure," *International Journal of Computational Fluid Dynamics*, Vol. 5, 1995, pp. 1–38.

[11]Steinhoff, J., *Frontiers of Computational Fluid Dynamics*, chap. 14 Vorticity Confinement: A New Technique for Computing Vortex Dominated Flows, John Wiley & Sons, 1994, pp. 235–263, eds. Caughey, D. A. & Hafez, M. M.

[12]Steinhoff, J. and Underhill, D., "Modification of Euler Equations for "Vorticity Confinement" – Application to the Computation of Interacting Vortex Rings," *Physics of Fluids*, Vol. 6, No. 8, 1994, pp. 2738–2744.

[13]Hu, G., Grossman, B., and J., S., "Numerical Method for Vorticity Confinement in Compressible Flow," *AIAA Journal*, Vol. 40, No. 10, 2002, pp. 1945–1953.

[14]Hu, G. and Grossman, B., "The Computational of Massively Separated Flows Using Compressible Vorticity Confinement Methods," *AIAA 40th Aerospace Sciences Meeting & Exhibit*, Reno, NV, January 2002, AIAA Paper 2002–0714.

[15]Fedkiw, R., Stam, J., and Jensen, H. W., "Visual Simulation of Smoke," *International Conference on Computer Graphics and Interactive Techniques, Proceedings of the 28th Annual Conference on Computer Graphics and Interactive Techniques*, 2001, pp. 15–22.

[16]Löhner, R. and Yang, C., "Vorticity Confinement on Unstructured Grids," *AIAA 40th Aerospace Sciences Meeting & Exhibit*, Reno, NV, January 2002, AIAA Paper 2002–0137.

[17]Löhner, R., Yang, C., and Roger, R., "Tracking Vortices over Large Distances Using Vorticity Confinement," *24th Symposium on Naval Aerodynamics*, Fukuoka, Japan, July 2002.

[18]Robinson, M., "Application of Vorticity Confinement to Inviscid Missile Force and Moment Prediction," *AIAA 42nd Aerospace Sciences Meeting & Exhibit*, Reno, NV, January 2004, AIAA Paper 2004–0717.

[19]Caradonna, F. X., Laub, G. H., and Tung, C., "An Experimental Investigation of the Parallel Blade–Vortex Interaction," Tech. Rep. NASA Technical Memorandum 86005, National Aeronautics and Space Administration, November 1984.

[20]Caradonna, F. X. and Tung, C., "Experimental and Analytical Studies of a Model Helicopter Rotor in Hover," Tech. Rep. NASA Technical Memorandum 81232, National Aeronautics and Space Administration, September 1981.

[21]Allen, C. B., "An Unsteady Multiblock Multigrid Scheme for Lifting Forward Flight Rotor Simulation," *International Journal for Numerical Methods in Fluids*, Vol. 45, No. 9, 2004, pp. 973–984.

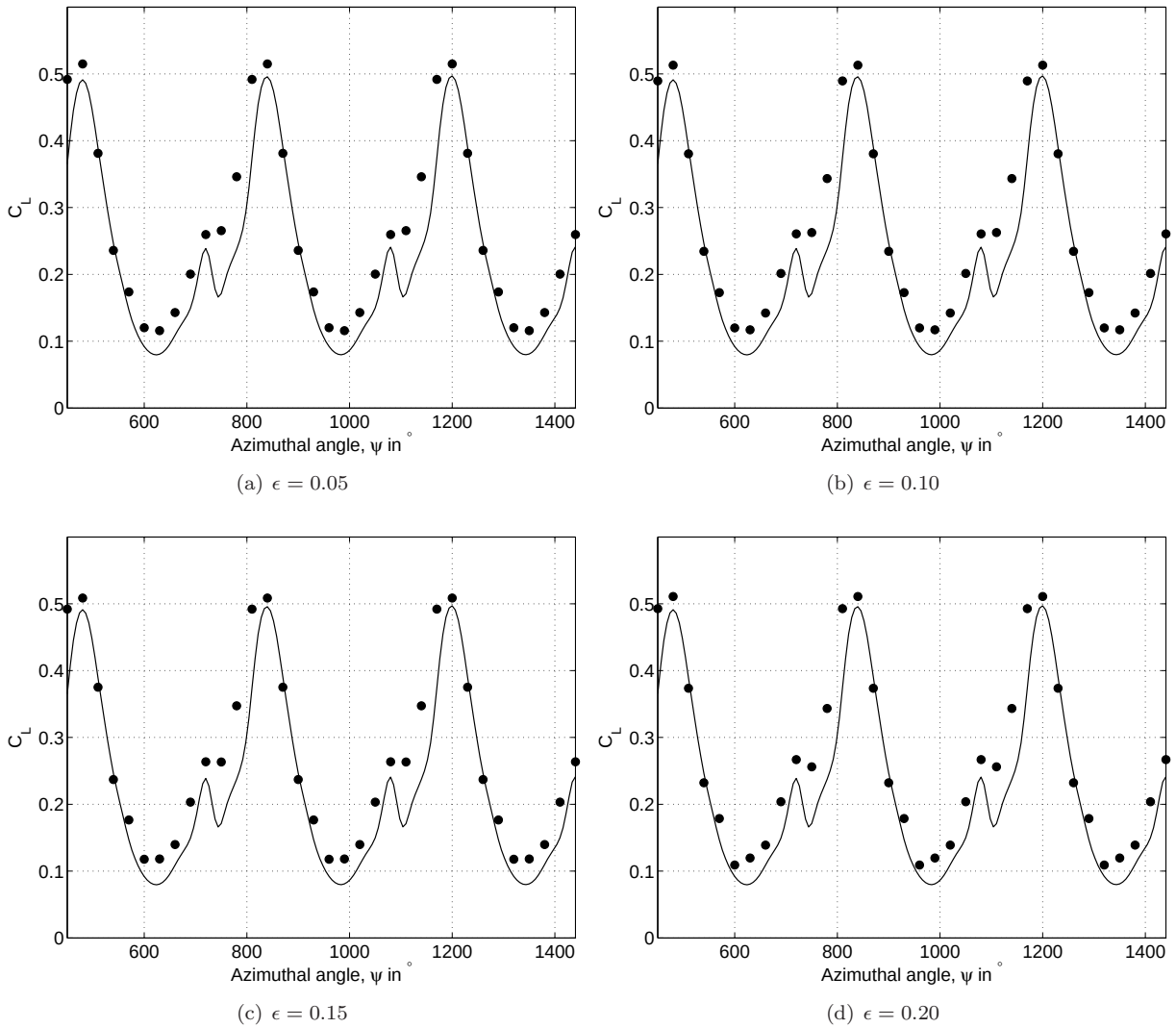

(a) $\epsilon = 0.05$ (b) $\epsilon = 0.10$

(c) $\epsilon = 0.15$ (d) $\epsilon = 0.20$

Figure 12. Coefficient of lift per blade vs. the azimuth of a lifting rotor in forward flight using Euler calculation with the JST dissipation scheme combined with Vorticity Confinement: $M_t = 0.7$, $\mu = 0.2857$, $\theta_c = 8^\circ$, $N = 12$, • computed result from the current work using the JST dissipation scheme with Vorticity Confinement, — simulation result provided Allen.

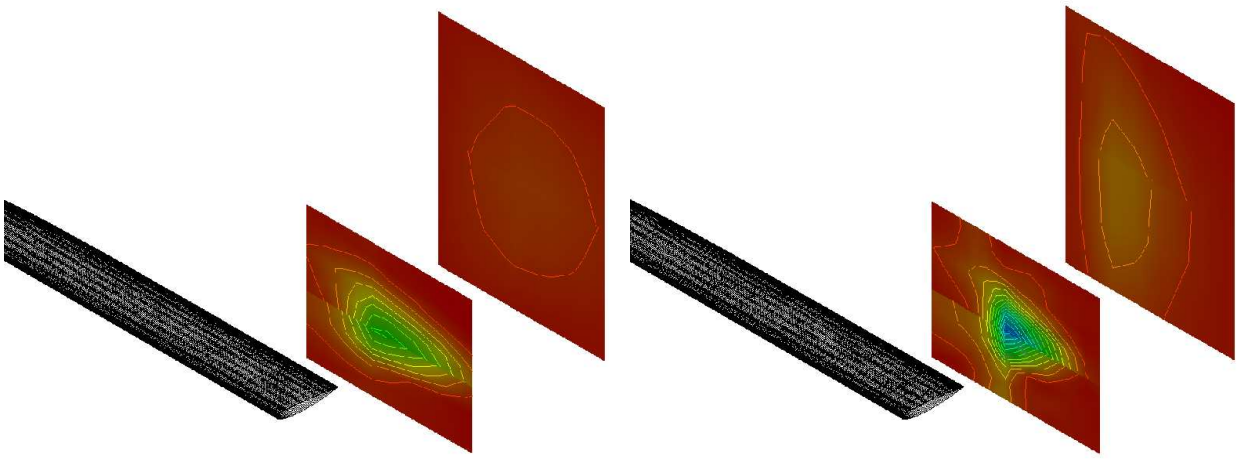

(a) $\epsilon = 0$ (b) $\epsilon = 0.2$

Figure 13. Vorticity magnitude of a lifting rotor in forward flight at the cut-planes $x = 2$ and $x = 5$ with $160 \times 48 \times 48$ mesh cells: $M_t = 0.7$, $\mu = 0.2857$, $\theta_c = 8^\circ$, $N = 12$, $\psi = 90^\circ$.

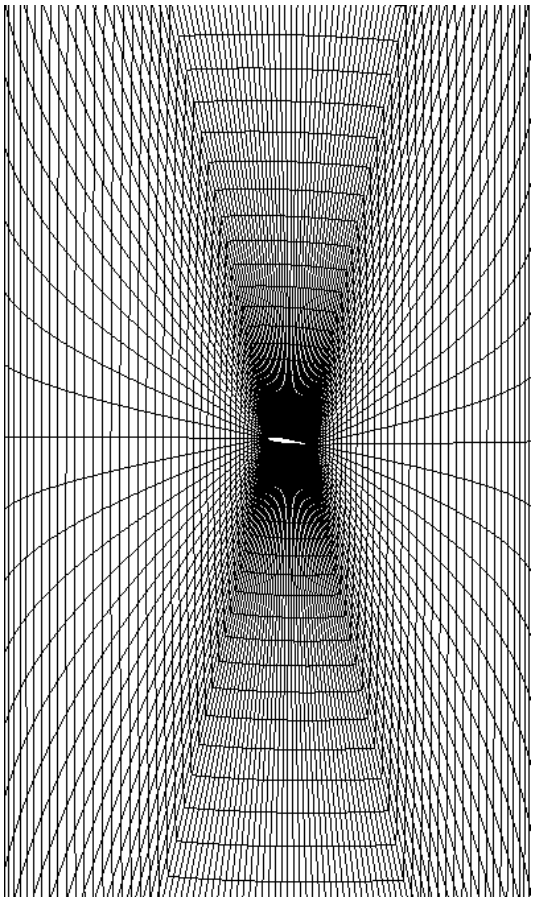

Figure 14. Mesh cross section at the tip of of the blade